# Designing Tripodal and Triangular Gadolinium Oxide Nanoplates and Self-Assembled Nanofibrils as Potential Multimodal Bioimaging Probes

Taejong Paik,[†] Thomas R. Gordon,[†] Andrew M. Prantner,[§] Hongseok Yun,[†] and Christopher B. Murray*,[†,‡]

[†]Department of Chemistry, University of Pennsylvania, Philadelphia, Pennsylvania 19104, United States, [‡]Department of Materials Science and Engineering, University of Pennsylvania, 3231 Walnut Street, Philadelphia, Pennsylvania 19104, United States, and [§]Penn Ovarian Cancer Research Center, Department of Obstetrics and Gynecology, University of Pennsylvania Perelman School of Medicine, Philadelphia, Pennsylvania 19104, United States

ABSTRACT Here, we report the shape-controlled synthesis of tripodal and triangular gadolinium oxide (Gd_2O_3) nanoplates. In the presence of lithium ions, the shape of the nanocrystals is readily controlled by tailoring reaction parameters such as temperature and time. We observe that the morphology transforms from an initial tripodal shape to a triangular shape with increasing reaction time or elevated temperatures. Highly uniform Gd_2O_3 nanoplates are self-assembled into nanofibril-like liquid-crystalline superlattices with long-range orientational and positional order. In addition, shape-directed self-assemblies are investigated by tailoring the aspect ratio of the arms of the Gd_2O_3 nanoplates. Due to a strong paramagnetic response, Gd_2O_3 nanocrystals are excellent candidates for MRI contrast agents and also can be doped with rare-earth ions to form nanophosphors, pointing to their potential in multimodal imaging. In this work, we investigate the MR relaxometry at high magnetic fields (9.4 and 14.1 T) and the optical properties including near-IR to visible upconversion luminescence and X-ray excited optical luminescence of doped Gd_2O_3 nanoplates. The complex shape of Gd_2O_3 nanoplates, coupled with their magnetic properties and their ability to phosphoresce under NIR or X-ray excitation which penetrate deep into tissue, makes these nanoplates a promising platform for multimodal imaging in biomedical applications.
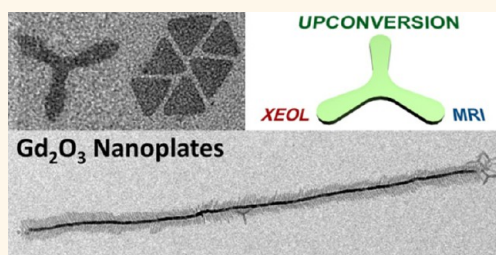
KEYWORDS: gadolinium oxide · tripod · MRI · contrast agent · XEOL · upconversion · nanophosphor

Establishing methods to synthesize nanocrystals with well-defined size and shape is crucial, as the size, shape, surface, and crystal structure all strongly influence the properties of nanocrystals.[1−3] Synthesis of nanocrystals with tailored morphology allows for correlation of the optical, magnetic, and electronic properties with the nanocrystal size and shape. This insight guides the design of nanocrystals optimized for various applications.[4−7] Shape control of nanocrystals is achieved using various methods, including seed-mediated growth,[8] control of reaction kinetics,[9,10] selective passivation by surfactants,[11,12] oriented attachment,[13] and sequential cation exchange processes.[14,15] Using these strategies, the morphology of nanocrystals has expanded to include nanorods,[16] nanowires,[17] nanoplates,[18] nanocubes,[19] multipods,[20] and other faceted nanocrystals.[21,22]

Anisotropic nanocrystals with precisely designed size and shape provide new types of building blocks for anisotropic superstructures.[23−27] Building blocks with anisotropic shapes or surface interactions enrich the structural diversity of nanocrystal superlattices by allowing for shape-directed self-assembly.[28] These superstructures are particularly interesting because they resemble a variety of biological structures which are created by the directed self-assembly of small molecules or a hierarchical coassembly of ordered structures. For example, the unidirectional self-assembly of anisotropic nanocrystals is reminiscent of the formation of fibrils, which are a major structural building block of biomaterials such as skin, tendon, bone, and other connective tissues.[29,30] Self-assembled superlattices can mimic complex biomaterials, acting as models to understand

the process by which biomaterials self-organize and the structure–property relationships.[31]

In biomedical research and clinical medicine, nanocrystals and their assembled structures play an increasingly important role as imaging agents.[32,33] Nanocrystal-based imaging probes can offer enhanced sensitivity and spatial resolution through incorporation of two or more imaging modalities into a single nanocrystal.[34–37] The properties of nanocrystals may be further manipulated through controlled aggregation or self-assembly of individual nanocrystals *in vivo*.[38–40] Furthermore, the high surface area of nanocrystals facilitates their surface modification with targeting reagents, providing enhanced detection sensitivity and selective targeting of therapeutic agents.[41,42] While early studies focused on understanding how the physical properties of nanocrystals are modified by particle size and shape, evidence suggests that the size and shape of nanocrystals can also directly influence the interaction of nanocrystals with biological systems. The effect of nanocrystal size on enhanced permeability and retention (EPR) and *in vivo* blood circulation time is well-documented in the literature.[43–45] More recently, the nanocrystal shape was also shown to influence cellular internalization and nanoparticle–cell interaction.[46–51] For example, disk-shaped nanocrystals preferentially accumulate within tumor vasculature and increase the sensitivity of tumor detection.[52] This result indicates the importance of nanocrystal shape on biological interactions. Monodispersity is essential in this investigation because it allows for accurate analysis of biodistributions without the confounding effect of size-dependent clearance. Therefore, it is a prerequisite to develop methods to tune the morphology of highly uniform nanocrystals that can be directly applied as imaging agents.

Lanthanide-based nanocrystals are promising candidates for nanomedicine applications.[53–58] A rich morphological diversity of lanthanide-based nanophophors exists which may be tailored by precisely controlling reaction conditions.[59–63] Lanthanide ions have free f-electrons, which are responsible for their unique magnetic and optical properties, and allow for the design of customized nanocrystals by simply incorporating multiple lanthanide ions into the nanocrystals. The optical transition between f-orbitals is a parity forbidden transition, resulting in long excited state lifetimes (>1 μs). This facilitates energy transfer between atomic levels in doped lanthanide ions, which can result in nonlinear optical properties such as near-IR to visible two-photon upconversion.[64–67] In addition, lanthanide-based nanocrystals act as scintillating materials due to their high atomic number, providing an additional optical modality under high-energy radiation such as X-ray.[68–70] The paramagnetic behavior of several lanthanide elements, including Gd, enables the use of lanthanide-based materials as magnetic resonance imaging (MRI) contrast agents.

Here, we report shape-controlled synthesis of gadolinium oxide (Gd_2O_3) tripodal and triangular nanoplates. Gd_2O_3 is well-known as an MRI contrast imaging agent due its unique high spin paramagnetism.[71,72] Through simple addition of lithium hydroxide (LiOH), which is used as a shape-directing agent, highly uniform Gd_2O_3 nanoplates are synthesized with morphology tunable from a tripodal to a triangular shape. The complex morphology of the tripodal nanoplate, which resembles the 14.2 × 8.5 × 3.8 nm shape of an IgG antibody,[73] could provide an additional degree of freedom to tailor shape-dependent physiological interactions. In addition, we study near-IR to visible upconversion luminescence by codoping erbium (Er^{3+}) and ytterbium (Yb^{3+}) into the host and X-ray excited optical luminescence (XEOL) with europium (Eu^{3+}) or terbium (Tb^{3+}) dopants. Coupled with magnetic properties, tripodal and triangular Gd_2O_3 nanoplates can offer unique opportunities for multimodal imaging probes.

RESULTS AND DISCUSSION

Gadolinium oxide nanoplates are synthesized through thermal decomposition of gadolinium acetate precursors in the presence of lithium hydroxide. Lithium hydroxide is initially added to a nonpolar solvent mixture of oleic acid and 1-octadecene, and upon heating to 110 °C, lithium hydroxide reacts with oleic acid, likely forming lithium oleate, and becomes soluble in nonpolar media. After adding gadolinium acetate precursors, the reaction solution is heated to around 300 to 320 °C, resulting in the formation of Gd_2O_3 nanoplates. A high N_2 flow rate during the heating was found to be critical to synthesize uniform Gd_2O_3 nanoplates with the desired morphology. We propose that, upon heating, acetic acid formed from the acetate salts or decomposed components and water which volatilize in the reaction mixture can adversely affect the growing of nanocrystals.

Shape control of Gd_2O_3 nanoplates is achieved by controlling the reaction time and temperature. Figure 1 displays transmission electron microscope (TEM) images of Gd_2O_3 nanoplates synthesized at different temperatures. Gd_2O_3 nanoplates with tripodal plate morphology are formed after 1 h at 300 °C (Figure 1a). At a reaction temperature of 320 °C, with the same reaction time, triangular-shaped nanoplates are obtained as the final product (Figure 1b). Tripodal nanoplates show remarkable uniformity with narrow distributions even in the arm length and width (Figure 2). In addition, pure tripods are obtained exclusively without any other shape impurities, such as rods, bipods, or spheres. In some regions, tripodal nanoplates are observed to form liquid-crystalline superstructures with long-range order due to size and shape uniformity. Lithium ions play an important role in the formation of tripod morphology. When sodium ions
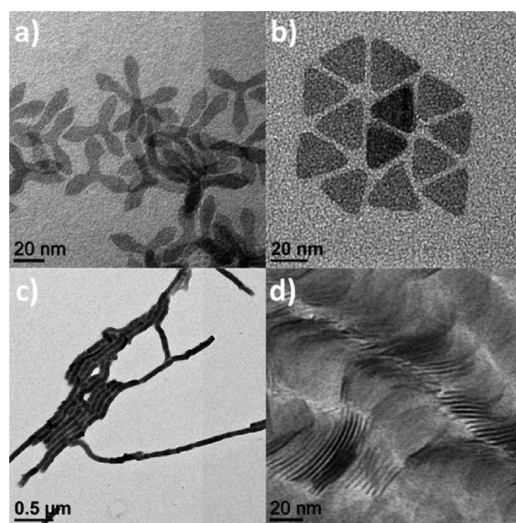
Figure 1. TEM images of Gd_2O_3 synthesized in the presence of LiOH: (a) Tripodal nanoplates and (b) triangular nanoplates. (c,d) Self-assembled Gd_2O_3 nanodisks synthesized in the presence of NaOH.

are used instead of lithium salts, disk-shaped ultrathin nanoplates are formed exclusively without any tripod or multipod morphologies (Figure 1c,d).

The crystal structure of Gd_2O_3 is characterized by powder X-ray diffraction (PXRD) and electron microscopy. Figure 3a displays the PXRD of tripodal and triangular Gd_2O_3 nanoplates. The crystal structure of plate-shaped Gd_2O_3 nanoplates most closely resembles the cubic phase bixbyite structure (JCPDS No. 43-1014). Similarity of peak broadening and intensity in diffraction patterns of two different shapes indicates that the crystallographic structure of the tripodal and triangular nanoplates is maintained during the morphological transformation. Both nanoplates show a sharp (440) reflection in PXRD patterns and broad peaks for the other planes, suggesting that the (440) plane lies in the plane of the nanoplates. Figure 3b,c shows high-resolution transmission electron microscopy (HRTEM) images of tripodal and triangular Gd_2O_3 nanoplates. Fast Fourier transforms of HRTEM images of these structures show single-crystalline patterns with six-fold symmetry. For a cubic crystal structure, this symmetry would only be shown from the [111] zone axis, indicating that our nanoplates are confined by the (111) plane and that growth occurs along the [110] direction. This description is consistent with the tripod morphology where three arms of a nanoplate form three-fold symmetry and correspond to the three equivalent {110} vectors in the [111] plane. In a previous report on Gd_2O_3 by Cao et al.[74] and an extended study of rare-earth oxide nanoplates,[60] it is reported that Gd_2O_3 nanoplates form a structure where the top and bottom planes of Gd_2O_3 nanoplates are enclosed by (001) planes with the c-axis as the direction of thickness. Compared to our experimental data, it is expected that addition of lithium may stabilize the (111) plane of Gd_2O_3

relative to the (100) plane, resulting in formation of nanoplate morphology truncated by the (111) plane.

Reflections of Gd_2O_3 nanoplates in PXRD patterns show deviations from the bulk peak positions. Measurement patterns show that expansion of interplanar distance along (222) and (400) planes is more distorted than in the (440) reflection peak. Size-dependent lattice expansion of metal oxide structure at the nanoscale is often observed with decreasing crystalline domain size smaller than 10 nm.[75] Our nanoplates are confined by the (222) plane, which means that a large portion of atoms in the (222) plane are located on the surface. Different atomic coordination of the surface atoms may induce a change in atomic bond length, which modifies the interplanar distance. In addition, due to the small size of the lithium ion, we anticipate that lithium may be doped into the Gd_2O_3 lattice, inducing lattice expansion, as similar results with sodium doping in rare-earth oxysulfide nanocrystals have been reported.[62]

A series of reactions conducted at a fixed reaction time but systematically varied reaction temperatures provide insight on the growth mechanism for tripodal and triangular nanoplates. At 280 °C and a 30 min reaction time, a mixture of nanorods and small round-shaped disks is observed, with a small portion of tripodal nanoplates (Figure 4a). After 1 h at 280 °C, a large portion of disks and rods are transformed into the tripod shape (Figure 4b). Careful inspection of nanoplates in the reaction at 280 °C reveals the formation of rod-shaped nanoplates with arrow-headed tips, which suggests that coalescence between small crystals may contribute to the growth in this early reaction. This is further supported by the observation of branched nanoplates in which additional branches grow from the center of the arms (Supporting Information Figure S1). Tripod nanoplates of high uniformity are the exclusive product when the reaction temperature is increased to 290 and 300 °C after a 1 h reaction time (Figure 4c,d). When the reaction temperature is increased to 310 °C, the aspect ratio of each arm decreases, forming a more triangular shape (Figure 4e). Triangular plates are exclusively observed after a 1 h reaction at 320 °C (Figure 4f).

To investigate the shape evolution of nanoplates, aliquots were taken during a single reaction and analyzed by TEM. Figure 5a−e represents TEM images of nanoplates taken at increasing time intervals for a 300 °C reaction temperature. Tripodal nanoplates are first formed after 1 h with tip-to-tip distance of 34 nm and a 2 nm thickness (Figures 5a and 3d). After aging at the same temperature, ripening occurs and induces a shape transformation in which the arm length decreases and the arm width increases. After 4 h, the morphology is completely transformed to a triangular shape with a 26 nm edge length and a 2 nm thickness (Figures 5b and 3e). The edge length of triangular plate is always smaller than the arm-to-arm length of tripodal plate,
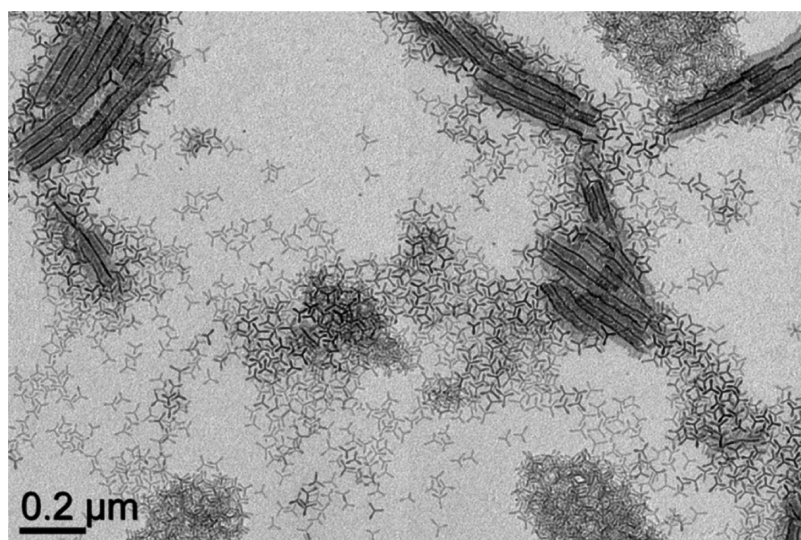
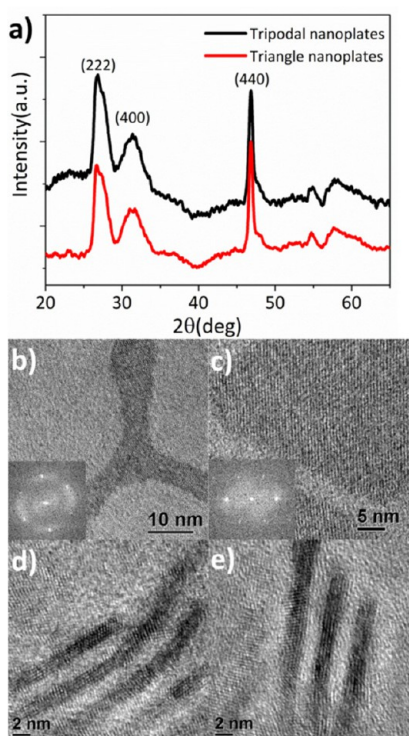**Figure 2. Low-magnification TEM image of Gd$_2$O$_3$ tripodal nanoplates.**

Figure 3. (a) Powder X-ray patterns of tripodal and triangular Gd$_2$O$_3$ nanoplates. High-resolution transmission electron microscopy (HRTEM) images of (b,d) tripodal and (c,e) triangular nanoplates. Insets are fast Fourier transforms of HRTEM images.

suggesting that this structural transformation is induced by atomic rearrangement of surface atoms to reduce the surface energy in the nanoplates, as illustrated in Figure 5f. All of the data indicate that branched nanoplates form at an early stage in the reaction, and the thermodynamically stable triangular shape results when sufficient energy is supplied to the reaction by increasing the reaction temperature or extending the reaction time. It is notable that the size and shape

uniformity is maintained throughout the whole shape transformation.

Due to the uniformity of the Gd$_2$O$_3$ nanoplates, self-assembly occurs to form 1-D nanofibril-like structures with long-range order (Figure 6a). All of the tripodal nanoplates that assemble into 1-D superlattices sit with two arms toward the substrate and one arm directed away from the substrate. The arms of the tripods align in perfect registry, which maximizes the interaction between nanoplates and forms a one-dimensional superlattice with an eclipsed conformation (Figure 6a). This structure is clearly visible in the scanning electron microscopy (SEM) images (Figure 6b).

One-dimensional nanofibril structures can be further aligned (bundled) together to form an extended ordered superstructure, which is commonly observed in the process of biomaterial formation. The size and shape uniformity of nanoplates allows us to demonstrate shape-directed self-assembly by tailoring the aspect ratio of arms of Gd$_2$O$_3$ nanoplates. In the case of tripodal nanoplates, nanofibril superlattices are organized into hierarchical superstructures. Each one-dimensional string (or nanofibril) is formed from the alignment of the constituent nanoplates, and these strings are bundled alternately into a superstructure by forming one string with two arms laying on the substrate and the inverted string with one arm contacting the substrate (Figure 6e, inset). For the shape intermediate between the tripodal and triangular plate with decreasing the aspect ratio of arms, two one-dimensional nanofibril structures tend to self-assemble through tip-to-tip contact of two arms (Figure 6f). Pure triangular nanoplates are ordered into columnar (Figure 6g) and lamellar (Figure 6h) liquid-crystalline superlattices by tiling of the nanoplate building blocks. Assembled superlattices of tripodal nanoplates contain free space between the two inverted nanofibril structures, forming
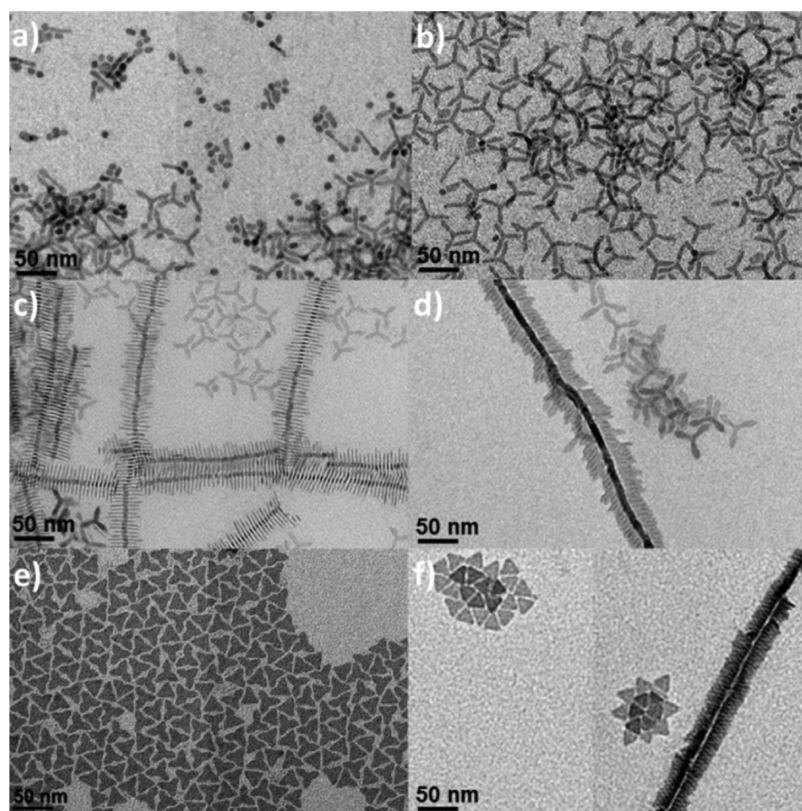
Figure 4. Temperature-dependent shape transformation. TEM images of nanoplates synthesized at (a) 280 °C for 30 min, (b) 280 °C, (c) 290 °C, (d) 300 °C, (e) 310 °C, (f) 320 °C for 1 h.

an open framework that is analogous to mesoporous structures. On the other hand, triangular nanoplates tend to be packed more efficiently, leaving minimal space except for the surface ligands (Figure 6f—h).

Through proper choice of optically active dopants, tripodal Gd_2O_3 nanoplates with minimal change in particle morphology can fluoresce under excitation by a variety of external energy sources, offering an optical imaging modality. Upconverting Gd_2O_3 tripodal nanoplates are synthesized through an addition of erbium (Er^{3+}) and ytterbium (Yb^{3+}) co-dopants. This tripodal upconverter shows near-IR to visible upconversion luminescence. Figure 7a shows upconversion luminescence spectra of 2% Er^{3+}, 20% Yb^{3+} co-doped Gd_2O_3 nanoplates under 980 nm irradiation. Characteristic green and red emission peaks are observed under near-IR excitation, located at 522, 542, and 656 nm, corresponding to $^2H_{11/2} \rightarrow {}^4I_{15/2}$, $^4S_{3/2} \rightarrow {}^4I_{15/2}$, and $^4F_9 \rightarrow {}^4I_{15/2}$ transitions of Er^{3+}, respectively. Upon introduction of europium (Eu^{3+}) or terbium (Tb^{3+}) dopants, Gd_2O_3 tripodal nanoplates can also exhibit an XEOL signature. Lanthanide-based scintillators are widely used for X-ray detectors due to their intrinsic high conversion efficiency from X-ray to visible light. Commercial terbium-doped gadolinium oxysulfide nanophosphors produce 6000 photons on average per each 100 keV X-ray photon absorbed.[76,77] To characterize the emission properties under high-energy excitation,

emission spectra were collected in an X-ray diffractometer using an optical fiber optically coupled to CCD from a sample under Cu Kα X-ray excitation ($\lambda = 1.5416$ Å). Figure 7b displays the emission spectrum of Tb^{3+}- and Eu^{3+}-doped Gd_2O_3 nanoplates under X-ray excitation. Depending on the dopant type, green and red emission peaks corresponding f—f transition of Tb^{3+} and Eu^{3+}, respectively, are observed, confirming that Tb^{3+}- or Eu^{3+}-doped Gd_2O_3 tripodal nanoplates can convert X-ray energy into visible light. Near-IR and X-ray photons show superb penetration into biological media, suggesting the possibility of utilizing these nanocrystals as efficient energy converters for *in vivo* applications.

To demonstrate the capability of Gd_2O_3 nanoplates to provide MR contrast in aqueous media, we performed a ligand exchange reaction because the as-synthesized hydrophobic nanoplates are stabilized by long alkyl chain surfactants. Water-soluble polyethyleneimine (PEI)-coated Gd_2O_3 nanoplates are prepared using a two-step ligand exchange process in which the tetrafluoroborate anion (BF_4^-) acts as an intermediate capping group. Figure 8 presents Fourier transform infrared (FT-IR) spectra of untreated, BF_4^--treated, and PEI-treated Gd_2O_3 nanoplates. After the first ligand exchange process with $NOBF_4$, the C—H stretching vibrations at 2800—3000 cm^{-1} are completely removed, indicating that the original surfactants are efficiently exchanged with the BF_4^- ligand. The weak binding
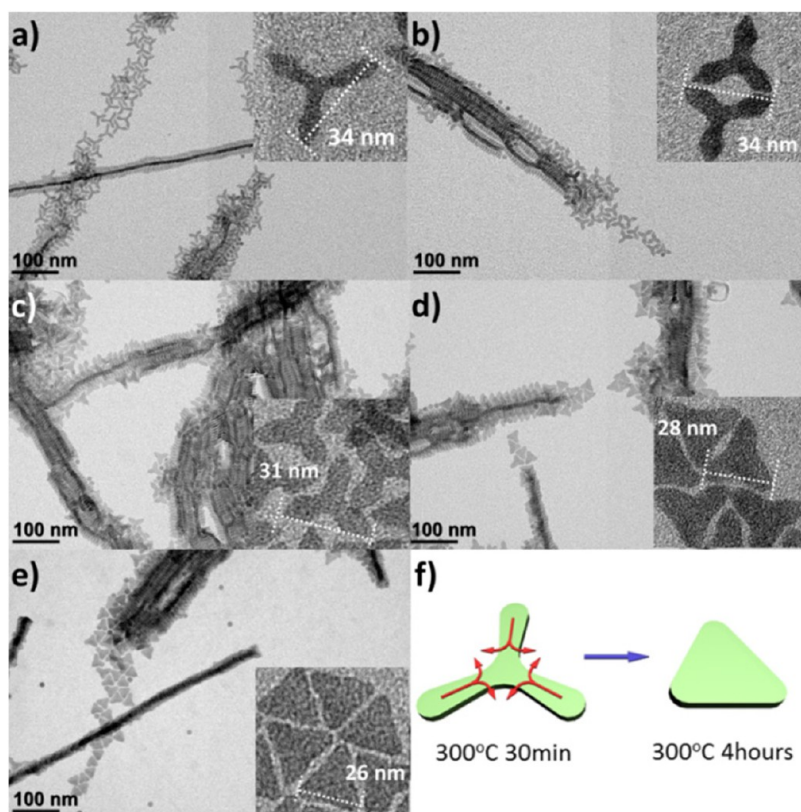
Figure 5. Reaction time-dependent shape transformation. TEM images of nanoplates synthesized at 300 °C for (a) 30 min, (b) 1 h, (c) 2 h, (d) 3 h, (e) 4 h. (f) Schematic of the nanoplate shape transformation.
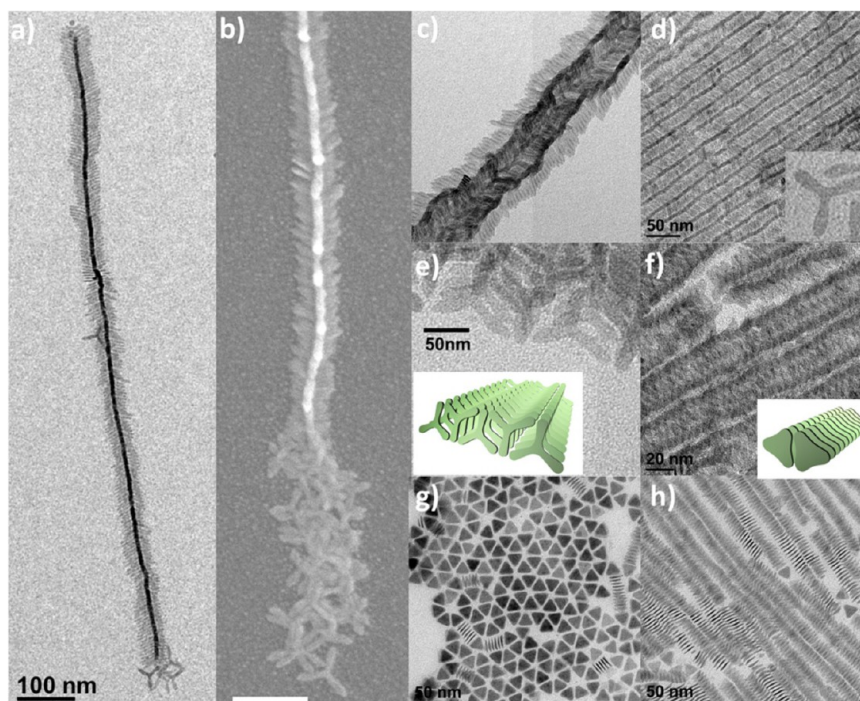

Figure 6. Microscopic images of shape-directed self-assembly of Gd$_2$O$_3$ nanoplates. (a) TEM and (b) SEM of one-dimensional self-assembly of tripodal nanoplates with eclipsed conformation. Scale bar is 100 nm. (c) Hierarchical self-assembled structure composed of three nanofibril structures. (d) Two-dimensional self-assembly and (e) high-magnification TEM of two-dimensional self-assembly of tripodal nanoplate. Inset is a schematic model of the ordered structure. (f) Liquid-crystalline self-assembly of tripodal nanoplates of smaller aspect ratio. Inset is a schematic model of the ordered structure. Self-assemblies of triangular nanoplates into (g) columnar and (h) lamellar liquid-crystalline superlattices.
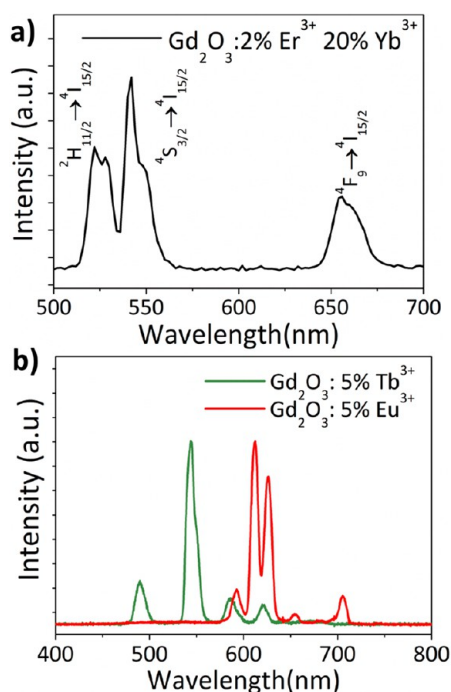
Figure 7. (a) Upconversion luminescence spectra of Er^{3+}, Yb^{3+} co-doped Gd_2O_3 nanoplates under 980 nm excitation. (b) X-ray excited optical luminescence spectra of Eu^{3+}- and Tb^{3+}-doped Gd_2O_3 nanoplates excited by Cu Kα X-ray irradiation.
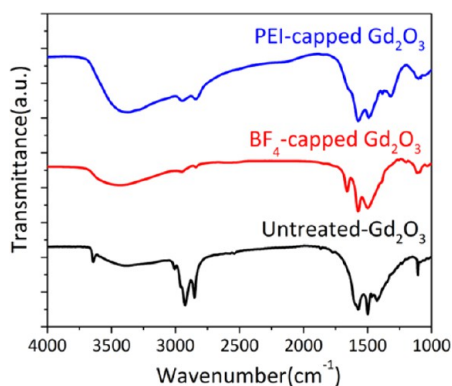

Figure 8. FT-IR spectra of Gd_2O_3 tripodal nanoplates before and after ligand exchange with BF_4^- and PEI.

affinity of BF_4^- ligands to the nanocrystal surface allows for efficient secondary surface modification using the PEI ligand. The occurrence of C—H vibrations after the second ligand exchange process with PEI, due to the C—H moiety in PEI molecules, indicates that the surfaces of the nanoplates are overcoated by PEI ligands. PEI-capped Gd_2O_3 is highly transparent and shows long-term colloidal stability without any noticeable precipitation in water.

The ionic relaxivity plots of PEI-capped Gd_2O_3 tripodal nanoplates at 9.4 and 14.1 T magnet are shown in Figure 9. The calculated longitudinal relaxivity (r_1) decreases from 1.41 to 0.89 mM^{-1} s^{-1}, and the transverse relaxivity (r_2) increases from 140 to 193 mM^{-1} s^{-1}
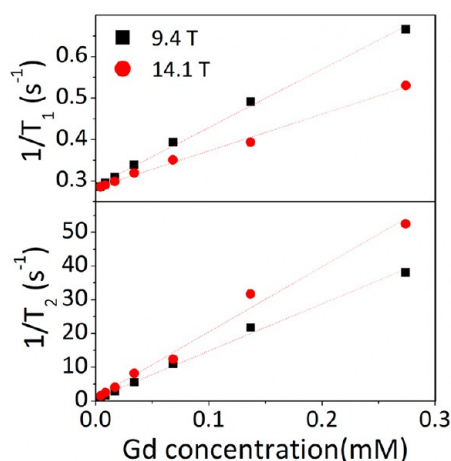

Figure 9. Longitudinal (top) and transverse (bottom) relaxivity curves of tripodal nanoplates.

TABLE 1. Relaxivites r_1 and r_2 of Gd_2O_3 Tripodal Nanoplate at 9.4 and 14.1 T Magnetic Field

	r_1 (mM^{-1} s^{-1})	r_2 (mM^{-1} s^{-1})	r_2/r_1
9.4 T	1.41	140	99.3
14.1 T	0.89	193	217

with an increase in magnetic field strength (Table 1), which is consistent with a previous report.[78] Reduced spectral density at higher magnetic field strengths results in less efficient dipole—dipole relaxation and a corresponding decrease in r_1. The transverse relaxivity, r_2, increases as the magnetic field strength goes from 9.4 to 14.1 T due to more effective dephasing of the transverse magnetization as a result of larger local magnetic fields, which are proportional to the magnetic moment of the paramagnetic nanoparticles. As a result, the r_2/r_1 value increases from 99.3 at 9.4 T to 217 at 14.1 T, which makes Gd_2O_3 tripodal nanoplates promising candidates for increasing the detection sensitivity of various pathologies in T_2- and T_2*-weighted images collected at higher magnetic fields now available for preclinical and clinical MRI.

CONCLUSION

In summary, shape-controlled synthesis of tripodal and triangular gadolinium oxide (Gd_2O_3) nanoplates has been demonstrated. Through addition of lithium ions to the reaction, tripodal- and triangular-shaped Gd_2O_3 nanoplates are synthesized with high size and shape uniformity. We observe that tripodal nanoplates form at an early reaction stage and transform into a triangular shape when the reaction temperature is increased or the reaction time is extended. Highly uniform Gd_2O_3 nanoplates self-assembled into 1-D nanofibril-like superlattices. In addition, the nanofibril structures can be further assembled into liquid-crystalline superstructures. We demonstrate that our

tripodal nanoplates exhibit two-photon upconversion luminescence when doped with Er^{3+} and Yb^{3+}. In addition, when doped with Eu^{3+} or Tb^{3+}, characteristic visible emission is observed under X-ray excitation, allowing this material to also function as a down-converter (scintillator) which converts high-energy radiation into visible light. We also investigate the MR relaxometry of Gd_2O_3 tripodal nanoplates at high magnetic fields, 9.4 and 14.1 T. At the higher magnetic field, the transverse relaxation rate of tripodal nanoplates increases, enhancing the r_2/r_1 ratio.

EXPERIMENTAL SECTION

Materials. All chemicals are used as purchased without any further purification. Gadolinium(III) oxide (99.99%), erbium(III) oxide (99.9%), terbium(III) oxide (99.9%), europium(III) oxide (99.9%), ytterbium(III) oxide (99.99%), oleic acid (technical grade, 90%), oleylamine (technical grade, 70%), 1-octadecene (technical grade, 90%), and lithium hydroxide monohydrate (99.95%) are purchased from Sigma Aldrich. Lanthanide acetate precursors are prepared by refluxing lanthanide oxide in acetic acid/water mixture (50 vol %).

Synthesis of Gd_2O_3 Nanoplates. Lithium hydroxide (6 mmol) is added into a mixture of 12 mL of oleic acid, 18 mL of oleylamine, and 30 mL of 1-octadecene solvent and is heated to 110 °C. After evacuation at 110 °C for 1 h to remove water, 3 mmol of gadolinium acetate is added and the solution is evacuated for an extra hour at the same temperature. Then, the reaction solution is heated between 300 and 320 °C for 1 h under high N_2 blowing, resulting in the formation of the nanoplates. The reaction solution is cooled to room temperature through addition of toluene. Purification is conducted through addition of excess methanol and centrifuging at 3000 rpm for 2 min.

Preparation of Water-Soluble Gd_2O_3 Nanoplates. Water-soluble Gd_2O_3 nanoplates are prepared through sequential ligand exchange process using BF_4^- as an intermediate ligand. First, ligand exchange with $NOBF_4$ is performed, as described previously.[79] The resulting nanocrystals are soluble in polar solvent such as dimethyl formamide (DMF) or dimethyl sulfoxide (DMSO). Secondary ligand exchange process is conducted with polyethyleneimine as a water-soluble ligand. Other water-soluble polymers such as polyvinylpyrrolidone (PVP) and poly(acrylic acid) (PAA) can be used instead. Two milliliters of nanocrystal solution in DMSO (0.1 mg nanocrystals/mL) is slowly added over 5 min into 2 mL of polyethyleneimine solution in DMSO (0.5 mg/mL concentration) and is stirred for 1 h. One milliliter of toluene is added to induce flocculation, and the particles are collected by centrifugation at 3000 rpm for 1 min. Diluted HCl solution is added into the nanocrystal solution to increase the colloidal stability.

Structure Characterization. TEM images and electron diffraction patterns are collected using a JEM-1400 microscope equipped with a SC1000 ORIUS CCD camera operating at 120 kV. Powder X-ray diffraction is measured using a Rigaku Smartlab high-resolution diffractometer with Cu Kα radiation ($\lambda = 1.5416$ Å). X-ray excited optical luminescence is recorded using a fiber-optically coupled CCD (Ocean Optics USB-2000) using Cu Kα radiation (8.04 keV) generated from a 2.2 kW sealed tube generator. Upconversion luminescence is collected with Jovin Yvon Fluorolog-3 spectrofluorometer using a 980 nm diode laser (1.06 W power and a 0.05 W/mm^2 power density) as an excitation source.

Magnetic Resonance Measurements. Samples at different gadolinium concentrations were prepared in phosphate buffered saline containing 10% deuterium oxide. Gadolinium ion concentration is measured by inductively coupled plasma optical emission spectrometry (ICP-OES) on a SPECTRO GENESIS ICP spectrometer. An inversion recovery pulse sequence modified to account for radiation damping[80] and a Carr–Purcell–Meiboom–Gill pulse sequence are used to determine the T_1 and T_2 relaxation times at 9.4 and 14.1 T using a monoexponential fit of the signal intensities. The r_1 and r_2 relaxivites were calculated from a linear fit of the relaxation rate constant as a function of gadolinium concentration.[81]

Conflict of Interest: The authors declare no competing financial interest.

REFERENCES AND NOTES

1. Murray, C. B.; Kagan, C. R.; Bawendi, M. G. Synthesis and Characterization of Monodisperse Nanocrystals and Close-Packed Nanocrystal Assemblies. *Annu. Rev. Mater. Sci.* **2000**, *30*, 545–610.

2. Murphy, C. J.; Sau, T. K.; Gole, A. M.; Orendorff, C. J.; Gao, J.; Gou, L.; Hunyadi, S. E.; Li, T. Anisotropic Metal Nanoparticles: Synthesis, Assembly, and Optical Applications. *J. Phys. Chem. B* **2005**, *109*, 13857–13870.

3. Xia, Y.; Xiong, Y.; Lim, B.; Skrabalak, S. E. Shape-Controlled Synthesis of Metal Nanocrystals: Simple Chemistry Meets Complex Physics?. *Angew. Chem., Int. Ed.* **2008**, *48*, 60–103.

4. Jun, Y.-w.; Huh, Y.-M.; Cho, J.-s.; Lee, J.-H.; Song, H.-T.; Kim, S.; Yoon, S.; Kim, K.-S.; Shin, J.-S.; Suh, J.-S.; *et al.* Nanoscale Size Effect of Magnetic Nanocrystals and Their Utilization for Cancer Diagnosis *via* Magnetic Resonance Imaging. *J. Am. Chem. Soc.* **2005**, *127*, 5732–5733.

5. Kim, B. H.; Lee, N.; Kim, H.; An, K.; Park, Y. I.; Choi, Y.; Shin, K.; Lee, Y.; Kwon, S. G.; Na, H. B.; *et al.* Large-Scale Synthesis of Uniform and Extremely Small-Sized Iron Oxide Nanoparticles for High-Resolution T_1 Magnetic Resonance Imaging Contrast Agents. *J. Am. Chem. Soc.* **2011**, *133*, 12624–12631.

6. Tromsdorf, U. I.; Bruns, O. T.; Salmen, S. C.; Beisiegel, U.; Weller, H. A Highly Effective, Nontoxic T_1 MR Contrast Agent Based on Ultrasmall PEGylated Iron Oxide Nanoparticles. *Nano Lett.* **2009**, *9*, 4434–4440.

7. Dong, A.; Chen, J.; Vora, P. M.; Kikkawa, J. M.; Murray, C. B. Binary Nanocrystal Superlattice Membranes Self-Assembled at the Liquid–Air Interface. *Nature* **2010**, *466*, 474–477.

8. Nikoobakht, B.; El-Sayed, M. A. Preparation and Growth Mechanism of Gold Nanorods (NRs) Using Seed-Mediated Growth Method. *Chem. Mater.* **2003**, *15*, 1957–1962.

9. Petroski, J. M.; Wang, Z. L.; Green, T. C.; El-Sayed, M. A. Kinetically Controlled Growth and Shape Formation Mechanism of Platinum Nanoparticles. *J. Phys. Chem. B* **1998**, *102*, 3316–3220.

10. Xiong, Y.; McLellan, J. M.; Chen, J.; Yin, Y.; Li, Z.-Y.; Xia, Y. Kinetically Controlled Synthesis of Triangular and Hexagonal Nanoplates of Palladium and Their SPR/SERS Properties. *J. Am. Chem. Soc.* **2005**, *127*, 17118–17127.

11. Huang, J.; Kovalenko, M. V.; Talapin, D. V. Alkyl Chains of Surface Ligands Affect Polytypism of CdSe Nanocrystals and Play an Important Role in the Synthesis of Anisotropic Nanoheterostructures. *J. Am. Chem. Soc.* **2010**, *132*, 15866.

12. Gao, J.; Bender, C. M.; Murphy, C. J. Dependence of the Gold Nanorod Aspect Ratio on the Nature of the Directing Surfactant in Aqueous Solution. *Langmuir* **2003**, *19*, 9065–9070.

13. Cho, K.-S.; Talapin, D. V.; Gaschler, W.; Murray, C. B. Designing PbSe Nanowires and Nanorings through Oriented Attachment of Nanoparticles. *J. Am. Chem. Soc.* **2005**, *127*, 7140–7147.

14. Son, D. H.; Hughes, S. M.; Yin, Y.; Alivisatos, A. P. Cation Exchange Reactions in Ionic Nanocrystals. *Science* **2004**, *306*, 1009–1012.

15. Deka, S.; Miszta, K.; Dorfs, D.; Genovese, A.; Bertoni, G.; Manna, L. Octapod-Shaped Colloidal Nanocrystals of Cadmium Chalcogenides *via* "One-Pot" Cation Exchange and Seeded Growth. *Nano Lett.* **2010**, *10*, 3770–3776.

16. Jana, N. R.; Gearheart, L.; Murphy, C. J. Wet Chemical Synthesis of High Aspect Ratio Cylindrical Gold Nanorods. *J. Phys. Chem. B* **2001**, *105*, 4065–4067.

17. Sun, Y.; Xia, Y. Large-Scale Synthesis of Uniform Silver Nanowires through a Soft, Self-Seeding, Polyol Process. *Adv. Mater.* **2002**, *14*, 833–837.

18. Sigman, M. B., Jr.; Ghezelbash, A.; Hanrath, T.; Saunders, A. E.; Lee, F.; Korgel, B. A. Solventless Synthesis of Monodisperse Cu_2S Nanorods, Nanodisks, and Nanoplatelets. *J. Am. Chem. Soc.* **2003**, *125*, 16050–16057.

19. Lee, N.; Choi, Y.; Park, Y. L. M.; Moon, W. K.; Choi, S. H.; Hyeon, T. Water-Dispersible Ferrimagnetic Iron Oxide Nanocubes with Extremely High r_2 Relaxivity for Highly Sensitive *In Vivo* MRI of Tumors. *Nano Lett.* **2012**, *12*, 3127–3131.

20. Manna, L.; Scher, E. C.; Alivisatos, A. P. Synthesis of Soluble and Processable Rod-, Arrow-, Teardrop-, and Tetrapod-Shaped CdSe Nanocrystals. *J. Am. Chem. Soc.* **2000**, *122*, 12700–12706.

21. Tao, A. R.; Habas, S.; Yang, P. Shape Control of Colloidal Metal Nanocrystals. *Small* **2008**, *4*, 310–325.

22. Burda, C.; Chen, X.; Narayanan, R.; El-Sayed, M. A. Chemistry and Properties of Nanocrystals of Different Shapes. *Chem. Rev.* **2005**, *105*, 1025–1102.

23. Grzelczak, M.; Vermant, J.; Furst, E. M.; Liz-Marzán, L. M. Directed Self-Assembly of Nanoparticles. *ACS Nano* **2010**, *4*, 3591–3605.

24. Huo, Z.; Tsung, C.-K.; Huang, W.; Fardy, M.; Yan, R.; Zhang, X.; Li, Y.; Yang, P. Self-Organized Ultrathin Oxide Nanocrystals. *Nano Lett.* **2009**, *9*, 1260–1264.

25. Jones, M. R.; Macfarlane, R. J.; Lee, B.; Zhang, J.; Young, K. L.; Senesi, A. J.; Mirkin, C. A. DNA-Nanoparticle Superlattices Formed from Anisotropic Building Blocks. *Nat. Mater.* **2010**, *9*, 913–917.

26. Paik, T.; Ko, D.-K.; Gordon, T. R.; Doan-Nguyen, V.; Murray, C. B. Studies of Liquid Crystalline Self-Assembly of GdF_3 Nanoplates by In-Plane, Out-of-Plane SAXS. *ACS Nano* **2011**, *5*, 8322–8330.

27. Miszta, K.; de Graaf, J.; Bertoni, G.; Dorfs, D.; Brescia, R.; Marras, S.; Ceseracciu, L.; Cingolani, R.; von Roij, R.; Dijkstra, M.; *et al.* Hierarchical Self-Assembly of Suspended Branched Colloidal Nanocrystals into Superlattice Structures. *Nat. Mater.* **2011**, *10*, 872–876.

28. Glotzer, S. C.; Solomon, M. J. Anisotropy of Building Blocks and Their Assembly into Complex Structures. *Nat. Mater.* **2007**, *6*, 557–562.

29. Zhang, S. Fabrication of Novel Biomaterials through Molecular Self-Assembly. *Nat. Biotechnol.* **2003**, *21*, 1171–1178.

30. Kadler, K. E.; Holmes, D. F.; Trotter, J. A.; Chapman, J. A. Collagen Fibril Formation. *Biochem. J.* **1996**, *316*, 1–11.

31. Hartgerink, J. D.; Beniash, E.; Stupp, S. I. Self-Assembly and Mineralization of Peptide-Amphiphile Nanofibers. *Science* **2001**, *294*, 1684–1688.

32. Michalet, X.; Pinaud, F. F.; Bentolila, L. A.; Tsay, J. M.; Doose, S.; Li, J. J.; Sundaresan, G.; Wu, A. M.; Gambhir, S. S.; Weiss, S. Quantum Dots for Live Cells, *In Vivo* Imaging, and Diagnostics. *Science* **2005**, *307*, 538–544.

33. Gao, X.; Cui, Y.; Levenson, R. M.; Chung, L. W. K.; Nie, S. *In Vivo* Cancer Targeting and Imaging with Semiconductor Quantum Dots. *Nat. Biotechnol.* **2004**, *22*, 969–976.

34. Cheon, J.; Lee, J.-H. Synergistically Integrated Nanoparticles as Multimodal Probes for Nanobiotechnology. *Acc. Chem. Res.* **2008**, *41*, 1630–1640.

35. Choi, J.-s.; Park, J. C.; Nah, H.; Woo, S.; Oh, J.; Kim, K. M.; Cheon, G. J.; Chang, Y.; Yoo, J.; Cheon, J. A Hybrid Nanoparticle Probe for Dual-Modality Positron Emission Tomography and Magnetic Resonance Imaging. *Angew. Chem., Int. Ed.* **2008**, *47*, 6259–6262.

36. Hao, R.; Xing, R.; Xu, Z.; Hou, Y.; Gao, S.; Sun, S. Synthesis, Functionalization, and Biomedical Applications of Multifunctional Magnetic Nanoparticles. *Adv. Mater.* **2010**, *22*, 2729–2742.

37. Haase, M.; Schäfer, H. Upconverting Nanoparticles. *Angew. Chem., Int. Ed.* **2011**, *50*, 5808–5829.

38. Pöselt, E.; Kloust, H.; Tromsdorf, U.; Janschel, M.; Hahn, C.; Maßlo, C.; Weller, H. Relaxivity Optimization of a PEGylated Iron-Oxide-Based Negative Magnetic Resonance Contrast Agent for T_2-Weighted Spin-Echo Imaging. *ACS Nano* **2012**, *6*, 1619–1624.

39. Yoon, T.-J.; Lee, H.; Shao, H.; Hilderbrand, S. A.; Weissleder, R. Multicore Assemblies Potentiate Magnetic Properties of Biomagnetic Nanoparticles. *Angew. Chem., Int. Ed.* **2011**, *23*, 4793–4797.

40. Perez, J. M.; Josephson, L.; O'Loughlin, T.; Högemann, D.; Weissleder, R. Magnetic Relaxation Switches Capable of Sensing Molecular Interactions. *Nat. Nanotechnol.* **2002**, *20*, 816–820.

41. Kim, J.; Piao, Y.; Hyeon, T. Multifunctional Nanostructured Naterials for Nultimodal Imaging, and Simultaneous Imaging and Therapy. *Chem. Soc. Rev.* **2009**, *38*, 372–390.

42. Yoo, D.; Lee, J.-H.; Shin, T.-H.; Cheon, J. Theranostic Magnetic Nanoparticles. *Acc. Chem. Res.* **2011**, *44*, 863–874.

43. Matsumura, Y.; Maeda, H.; New, A. Concept for Macromolecular Therapeutics in Cancer Chemotherapy: Mechanism of Tumoritropic Accumulation of Proteins and the Antitumor Agent Smancs. *Cancer Res.* **1986**, *46*, 6387–6392.

44. Maeda, H.; Wua, J.; Sawaa, T.; Matsumurab, Y.; Horic, K. Tumor Vascular Permeability and the EPR Effect in Macromolecular Therapeutics: A Review. *J. Controlled Release* **2000**, *65*, 271–284.

45. Jiang, W.; Kim, B. Y. S.; Rutka, J. T.; Chan, W. C. W. Nanoparticle-Mediated Cellular Response Is Size-Dependent. *Nat. Nanotechnol* **2008**, *3*, 145–150.

46. Albanese, A.; Tang, P. S.; Chan, W. C. W. The Effect of Nanoparticle Size, Shape, and Surface Chemistry on Biological Systems. *Annu. Rev. Biomed. Eng.* **2012**, *14*, 1.

47. Muro, S.; Garnacho, C.; Champion, J. A.; Leferovich, J.; Gajewski, C.; Schuchman, E. H.; Mitragotri, S.; Muzykantov, V. R. Control of Endothelial Targeting and Intracellular Delivery of Therapeutic Enzymes by Modulating the Size and Shape of ICAM-1-Targeted Carriers. *Mol. Ther.* **2008**, *16*, 1450–1458.

48. Gratton, S. E. A.; Ropp, P. A.; Pohlhaus, P. D.; Luft, J. C.; Madden, V. J.; Napier, M. E.; DeSimone, J. M. The Effect of Particle Design on Cellular Internalization Pathways. *Proc. Natl. Acad. Sci. U.S.A.* **2008**, *105*, 11613–11618.

49. Chithrani, B. D.; Ghazani, A. A.; Chan, W. C. W. Determining the Size and Shape Dependence of Gold Nanoparticle Uptake into Mammalian Cells. *Nano Lett.* **2006**, *6*, 662–668.

50. Qiua, Y.; Liua, Y.; Wanga, L.; Xua, L.; Baia, R.; Jib, Y.; Wub, X.; Zhaoa, Y.; Lic, Y.; Chen, C. Surface Chemistry and Aspect Ratio Mediated Cellular Uptake of Au Nanorods. *Biomaterials* **2010**, *31*, 7606–7619.

51. Zhang, Y.; Tekobo, S.; Tu, Y.; Zhou, Q.; Jin, X.; Dergunov, S. A.; Pinkhassik, E.; Yan, B. Permission to Enter Cell by Shape: Nanodisk *vs* Nanosphere. *ACS Appl. Mater. Interfaces* **2012**, *4*, 4099–4105.

52. Adriani, G.; de Tullio, M. D.; Ferrari, M.; Hussain, F.; Pascazio, G.; Liu, X.; Decuzzi, P. The Preferential Targeting of the Diseased Microvasculature by Disk-like Particles. *Biomaterials* **2012**, *33*, 5504.

53. Wang, F.; Liu, X. Recent Advances in the Chemistry of Lanthanide-Doped Upconversion Nanocrystals. *Chem. Soc. Rev.* **2009**, *38*, 976–989.

54. Zhoua, J.; Suna, Y.; Dub, X.; Xionga, L.; Hua, H.; Li, F. Dual-Modality *In Vivo* Imaging Using Rare-Earth Nanocrystals with Near-Infrared to Near-Infrared (NIR-to-NIR) Upconversion Luminescence and Magnetic Resonance Properties. *Biomaterials* **2010**, *31*, 3287–3295.

55. Wang, G.; Peng, Q.; Li, Y. Lanthanide-Doped Nanocrystals: Synthesis, Optical-Magnetic Properties, and Applications. *Acc. Chem. Res.* **2011**, *44*, 322–332.

56. Nyk, M.; Kumar, R.; Ohulchanskyy, T. Y.; Bergey, E. J.; Prasad, P. N. High Contrast *In Vitro* and *In Vivo* Photoluminescence Bioimaging Using Near Infrared to Near Infrared Upconversion in Tm^{3+} and Yb^{3+} Doped Fluoride Nanophosphors. *Nano Lett.* **2008**, *8*, 3834–3838.

57. Boyer, J.-C.; Manseau, M.-P.; Murray, J. I.; von Veggel, F. C. J. M. Surface Modification of Upconverting $NaYF_4$ Nanoparticles with PEG−Phosphate Ligands for NIR (800 nm) Biolabeling within the Biological Window. *Langmuir* **2010**, *26*, 1157–1164.

58. Das, G. K.; Johnson, N. J. J.; Cramen, J.; Blasiak, B.; Latta, P.; Tomanek, B.; von Veggel, F. C. J. M. $NaDyF_4$ Nanoparticles as T_2 Contrast Agents for Ultrahigh Field Magnetic Resonance Imaging. *J. Phys. Chem. Lett.* **2012**, *3*, 524–529.

59. Zhang, Q.; Yan, B. Hydrothermal Synthesis and Characterization of LiREF4 (RE = Y, Tb-Lu) Nanocrystals and Their Core−Shell Nanostructures. *Inorg. Chem.* **2010**, *49*, 6834–6839.

60. Si, R.; Zhang, Y.-W.; You, L.-P.; Yan, C.-H. Rare-Earth Oxide Nanopolyhedra, Nanoplates, and Nanodisks. *Angew. Chem., Int. Ed.* **2005**, *44*, 3256–3260.

61. Mai, H.-X.; Zhang, Y.-W.; Si, R.; Yan, Z.-G.; Sun, L.-d.; You, L.-P.; Yan, C.-H. High-Quality Sodium Rare-Earth Fluoride Nanocrystals: Controlled Synthesis and Optical Properties. *J. Am. Chem. Soc.* **2006**, *128*, 6426–6436.

62. Ding, Y.; Gu, J.; Ke, J.; Zhang, Y.-W.; Yan, C.-H. Sodium Doping Controlled Synthesis of Monodisperse Lanthanide Oxysulfide Ultrathin Nanoplates Guided by Density Functional Calculations. *Angew. Chem., Int. Ed.* **2011**, *50*, 12330–12334.

63. Wang, F.; Han, Y.; Lim, C. S.; Lu, Y.; Wang, J.; Xu, J.; Chen, H.; Zhang, C.; Hong, M.; Liu, X. Simultaneous Phase and Size Control of Upconversion Nanocrystals through Lanthanide Doping. *Nature* **2010**, *463*, 1061–1065.

64. Chatterjeea, D. K.; Rufaihaha, A. J.; Zhang, Y. Upconversion Fluorescence Imaging of Cells and Small Animals Using Lanthanide Doped Nanocrystals. *Biomaterials* **2008**, *29*, 937–943.

65. Boyer, J.-C.; Vetrone, F.; Cuccia, L. A.; Capobianco, J. A. Synthesis of Colloidal Upconverting $NaYF_4$ Nanocrystals Doped with Er^{3+}, Yb^{3+} and Tm^{3+}, Yb^{3+} *via* Thermal Decomposition of Lanthanide Trifluoroacetate Precursors. *J. Am. Chem. Soc.* **2006**, *128*, 7444–7445.

66. Wang, F.; Liu, X. Upconversion Multicolor Fine-Tuning: Visible to Near-Infrared Emission from Lanthanide-Doped $NaYF_4$ Nanoparticles. *J. Am. Chem. Soc.* **2008**, *130*, 5642–5643.

67. Heer, S.; Kömpe, K.; Güdel, H.-U.; Haase, M. Highly Efficient Multicolour Upconversion Emission in Transparent Colloids of Lanthanide-Doped $NaYF_4$ Nanocrystals. *Adv. Mater.* **2004**, *16*, 2102–2105.

68. Sun, C.; Pratx, G.; Carpenter, C. M.; Liu, H.; Cheng, Z.; Gambhir, S. S.; Xing, L. Synthesis and Radioluminescence of PEGylated Eu^{3+}-Doped Nanophosphors as Bioimaging Probes. *Adv. Mater.* **2011**, *23*, H195–H199.

69. Carpenter, C. M.; Sun, C.; Pratx, G.; Liu, H.; Cheng, Z.; Xing, L. Radioluminescent Nanophosphors Enable Multiplexed Small-Animal Imaging. *Opt. Express* **2012**, *20*, 11598–11604.

70. Liu, Y.; Chen, W.; Wang, S.; Joly, A. G.; Westcott, S.; Woo, B. K. X-ray Luminescence of LaF_3:Tb^{3+} and LaF_3:Ce^{3+},Tb^{3+} Water-Soluble Nanoparticles. *J. Appl. Phys.* **2008**, *2008*, 063105.

71. Bridot, J.-L.; Faure, A.-C.; Laurent, S.; Rivière, C.; Billotey, C.; Hiba, B.; Janier, M.; Josserand, V.; Coll, J.-L.; Elst, L. V.; *et al.* Hybrid Gadolinium Oxide Nanoparticles: Multimodal Contrast Agents for *In Vivo* Imaging. *J. Am. Chem. Soc.* **2007**, *129*, 5076–5084.

72. Johnson, N. J. J.; Oakden, W.; Stanisz, G. J.; Prosser, R. S.; von Veggel, F. C. J. M. Size-Tunable, Ultrasmall $NaGdF_4$ Nanoparticles: Insights into Their T^{-1} MRI Contrast Enhancement. *Chem. Mater.* **2011**, *23*, 3714–3722.

73. Sarma, V. R.; Silverton, E. W.; Davies, D. R.; Terry, W. D. The Three-Dimensional Structure at 6 Å Resolution of a Human γG1 Immunoglobulin Molecule. *J. Biol. Chem.* **1971**, *246*, 3753–3759.

74. Cao, Y. C. Synthesis of Square Gadolinium-Oxide Nanoplates. *J. Am. Chem. Soc.* **2004**, *126*, 7456–7457.

75. Tsunekawa, S.; Ito, S.; Kawazoe, Y. Surface Structures of Cerium Oxide Nanocrystalline Particles from the Size Dependence of the Lattice Parameters. *Appl. Phys. Lett.* **2004**, *85*, 3845.

76. Carpenter, C. M.; Sun, C.; Pratx, G.; Rao, R.; Xing, L. Hybrid X-ray/Optical Luminescence Imaging: Characterization of Experimental Conditions. *Med. Phys.* **2010**, *37*, 4011–4018.

77. Chen, H.; Patrick, A. L.; Yang, Z.; VanDerveer, D. G.; Anker, J. N. High-Resolution Chemical Imaging through Tissue with an X-ray Scintillator Sensor. *Anal. Chem.* **2011**, *83*, 5045–5049.

78. Norek, M.; Kampert, E.; Zeitler, U.; Peters, J. A. Tuning of the Size of Dy_2O_3 Nanoparticles for Optimal Performance as an MRI Contrast Agent. *J. Am. Chem. Soc.* **2008**, *130*, 5335–5340.

79. Dong, A.; Ye, X.; Chen, J.; Kang, Y.; Gordon, T.; Kikkawa, J. M.; Murray, C. B. A Generalized Ligand-Exchange Strategy Enabling Sequential Surface Functionalization of Colloidal Nanocrystals. *J. Am. Chem. Soc.* **2011**, *133*, 998–1006.

80. Eykyn, T. R.; Payne, G. S.; Leach, M. O. Inversion Recovery Measurements in the Presence of Radiation Damping and Implications for Evaluating Contrast Agents in Magnetic Resonance. *Phys. Med. Biol.* **2005**, *50*, N371–N376.

81. Lauffer, R. B. Paramagnetic Metal Complexes as Water Proton Relaxation Agents for NMR Imaging: Theory and Design. *Chem. Rev.* **1987**, *87*, 901–927.